ADVANCING EARTH AND SPACE SCIENCES

JGR Planets

RESEARCH ARTICLE
10.1029/2026JE009684

Nanophase Iron of New Nano-Lamella and Zoned Morphology Discovered in a Lunar Meteorite

Zhichen Zhao[1], Ruizhi Zhou[2], Renkang Song[1], Lihui Li[3,4], Zhou Zhou[1], Chao Wang[5], Wei Teng[6], Kunkun Fu[7], Zhengwu Jiang[8], Hengci Tian[9], Huan Xie[10], Yu Huang[2,11], Bofeng Li[10], Markus B. Raschke[12], Zhanshan Wang[1,11], Xiao Ma[13], Xiaohua Tong[10], Tao Jiang[1,11], and Hu Zheng[2,11]

[1]MOE Key Laboratory of Advanced Micro-Structured Materials, Shanghai Frontiers Science Center of Digital Optics, Institute of Precision Optical Engineering, and School of Physics Science and Engineering, Tongji University, Shanghai, China, [2]Department of Geotechnical Engineering, College of Civil Engineering, Tongji University, Shanghai, China, [3]State Key Laboratory of Lithospheric and Environmental Coevolution, Institute of Geology and Geophysics, Chinese Academy of Sciences, Beijing, China, [4]College of Earth and Planetary Sciences, University of Chinese Academy of Sciences, Beijing, China, [5]School of Materials Science and Engineering, Shanghai University, Shanghai, China, [6]State Key Laboratory of Water Pollution Control and Green Resource Recycling, College of Environmental Science and Engineering, Tongji University, Shanghai, China, [7]School of Aerospace Engineering and Applied Mechanics, Tongji University, Shanghai, China, [8]Key Laboratory of Advanced Civil Engineering Materials of Ministry of Education, School of Materials Science and Engineering, Tongji University, Shanghai, China, [9]Key Laboratory of Earth and Planetary Physics, Institute of Geology and Geophysics, Chinese Academy of Sciences, Beijing, China, [10]College of Surveying and Geo-Informatics, Tongji University, Shanghai, China, [11]Shanghai Institute of Intelligent Science and Technology, Tongji University, Shanghai, China, [12]Department of Physics, University of Colorado, Boulder, CO, USA, [13]Department of History of Science and Scientific Archaeology, University of Science and Technology of China, Hefei, China

Zhichen Zhao, Ruizhi Zhou, and Renkang Song contributed equally to this work.

Key Points:

- A unique form of nanoscale iron was discovered in the Fe-Ti-Cr minerals of a lunar basalt meteorite
- The iron exhibits a distinct three-layered structure characterized by three chemical states
- These observations offer new insight into the elementary processes of iron formation in lunar materials

Supporting Information:

Supporting Information may be found in the online version of this article.

Correspondence to:

T. Jiang and H. Zheng,
tjiang@tongji.edu.cn;
zhenghu@tongji.edu.cn

Citation:

Zhao, Z., Zhou, R., Song, R., Li, L., Zhou, Z., Wang, C., et al. (2026). Nanophase iron of new nano-lamella and zoned morphology discovered in a lunar meteorite. *Journal of Geophysical Research: Planets*, *131*, e2026JE009684. https://doi.org/10.1029/2026JE009684

Received 21 JAN 2026
Accepted 26 JUL 2026

Author Contributions:

Conceptualization: Tao Jiang, Hu Zheng
Investigation: Zhichen Zhao, Renkang Song, Zhou Zhou, Chao Wang
Methodology: Lihui Li, Xiao Ma
Resources: Hengci Tian, Xiaohua Tong
Supervision: Tao Jiang, Hu Zheng
Writing – original draft: Zhichen Zhao, Ruizhi Zhou
Writing – review & editing: Wei Teng, Kunkun Fu, Zhengwu Jiang, Huan Xie, Yu Huang, Bofeng Li, Markus B. Raschke, Zhanshan Wang, Tao Jiang, Hu Zheng

Abstract

Nanophase iron (np-Fe^0), as one of the key products of space weathering, is widely observed in the near-surface layer of lunar materials, providing crucial evidence for their geological evolution. Here we report the discovery of np-Fe^0 with a rare lamellar morphology, embedded in Fe-Ti-Cr oxide solid solutions within the interior of the lunar meteorite NWA 4734, characterized by nanometer-scale thicknesses and micrometer-scale lateral dimensions. Notably, these lamellae exhibit a unique three-layer core-shell structure, consisting of np-Fe^0 core, Fe^{3+}-bearing shell, and ilmenite-dominated outer layer. This finding offers new insights into the formation process of np-Fe^0 in lunar materials through thermal decomposition and disproportionation associated with impact events and space weathering, and reveals a novel pathway for nanomaterial synthesis under extreme conditions.

Plain Language Summary

Nanophase iron in lunar materials carries key information about surface processes on the Moon. In this study, we used multiple advanced, high-resolution imaging techniques to examine a basaltic lunar meteorite. Within the Fe-Ti-Cr minerals of the meteorite, we discovered a previously unrecognized nano-lamellar form of metallic iron. Formed under extreme conditions during large-scale impact events, these lamellae exhibit a distinct three-layered structure characterized by three different chemical states. The discovery demonstrates the formation of metallic iron deep within lunar materials attributed to impact events, contributing to the Moon's global iron inventory. This provides a new reference for the alteration of planetary materials under shock conditions, broadening our view of planetary history.

1. Introduction

Iron is one of the key elements for understanding the origin and geological evolution of the planets (Taylor & Konhauser, 2011; Johnson et al., 2008; Beard & Johnson, 2004). On Earth, it is rarely found in its native form and typically occurs in oxidized states within minerals. However, the Moon lacks a protective atmosphere and a global magnetic field, leading to continuous bombardment of its surface by micrometeorites and irradiation by the solar wind and cosmic rays (Mandt, 2024). Over geological timescales spanning millions to hundreds of millions of years, these processes have profoundly altered the mineralogy and surface structure of lunar regolith, imprinting enduring features such as nanophase iron (np-Fe^0) (Chen et al., 2024; J.-G. Guo et al., 2022; Z. Guo et al., 2022; Hapke, 2001; Keller & McKay, 1993, 1997; Li et al., 2022; Lu et al., 2023; Taylor et al., 2001; Sasaki et al., 2001; Shen et al., 2024; Thompson et al., 2016; K. Wang et al., 2012; Weber et al., 2020; Xian et al., 2023) and irradiation tracks (Comstock, 1977; Keller et al., 2021; Maurette & Price, 1975) that record its evolutionary history. The formation mechanisms of np-Fe^0 in lunar regolith are generally attributed to space weathering processes driven by evaporative deposition (Anand et al., 2004) and ionic reduction (Noguchi et al., 2011). The high-temperature and high-pressure conditions generated by the high speed impacts of micrometeorite can promote thermal evaporation and redeposition, resulting in the production of np-Fe^0 (Keller & McKay, 1993; Weber et al., 2020; Z. Guo et al., 2022). In contrast, solar wind irradiation induces ionic reduction of Fe-bearing phases through hydrogen implantation (Allen et al., 1993; Chen et al., 2024). Currently, np-Fe^0 formed through the aforementioned processes has been identified in lunar regolith, where it typically exists as nanoparticles embedded within amorphous rims and crater-like structures (Zeng et al., 2025). Such metallic nanostructures strongly affect the physical and chemical properties of planetary surfaces and are critical for the accurate analysis of the spectral characteristics through remote-sensing observations (DellaGiustina et al., 2020; Pieters et al., 2012).

The np-Fe^0 in the near-surface regions of lunar materials has been widely investigated as a product of space weathering and primarily reflects surface alteration processes. However, np-Fe^0 preserved within mineral interiors has the potential to record distinct geological processes relevant to planetary interiors, yet remains comparatively less explored. Shocked meteorites experienced extreme high-pressure and high-temperature conditions that led to the formation of np-Fe^0 within mineral interiors, providing invaluable natural analogues for examining the effects of large-scale impact events (Denevi et al., 2023; Li et al., 2022; Liu et al., 2025) and the incorporation of exotic meteorite components (Gopon et al., 2017; Lu et al., 2023; Warren et al., 1989) in planetary materials. The occurrence, abundance, and spatial distribution of np-Fe^0 and associated iron species in meteorites serve as important indicators of redox differentiation produced by impact-driven shock metamorphism within planetary interiors (Cao et al., 2024; Gu et al., 2025), and offer reference constraints for reconstructing conditions in the Earth's lower mantle (Bindi et al., 2020; Frost et al., 2004). Investigating the diverse formation pathways of np-Fe^0 provides a valuable window into the complex thermochemical evolution of planetary bodies.

Here we report the discovery of np-Fe^0 in the lunar meteorite NWA 4734, exhibiting an unusual lamellar morphology and a distinctive three-layer core-shell structure. Unlike the previously reported nanoparticle morphology near the surface, here np-Fe^0 occurs as continuous lamellar features with nanometer-scale thicknesses and micrometer-scale lateral dimensions, embedded within Fe-Ti-Cr oxide solid solutions, an underexplored Fe-bearing phase in lunar materials. We pursue a multimodal approach combining electron microscopy, X-ray spectroscopy, and nano-optical techniques to gain a complementary view of the nanostructure and composition of the lunar meteorite. Our results provide evidence that np-Fe^0 formed through thermal decomposition and disproportionation within Fe-Ti-Cr oxide solid solutions under shock metamorphism, and further reveal a three-layer structure comprising np-Fe^0 core, Fe^{3+}-bearing shell, and ilmenite-dominated outer layer. This discovery not only provides valuable implications for elucidating the formation mechanisms of np-Fe^0, which are essential for interpreting lunar geological evolution, but also offers new insights into the synthesis of metallic iron nanomaterials under extreme conditions.

2. Samples and Methods

The lunar material investigated in this study is the mare basalt meteorite NWA 4734. The meteorite samples were prepared by embedding the samples in an epoxy resin mount with a diameter of approximately 25.4 mm. Scanning electron microscopy (SEM) was employed to obtain an overview of sample textures and mineralogical compositions. Prior to SEM measurements, the mount was coated with a thin carbon layer to ensure electrical conductivity. SEM observations were carried out with a Zeiss Gemini 450 field-emission scanning electron microscope at the Institute of Geology and Geophysics, Chinese Academy of Sciences. The instrument was equipped with an Oxford Instruments ULTIM MAX 100 mm^2 silicon drift detector, enabling simultaneous imaging and energy-dispersive X-ray spectroscopy (EDS) analyses. Backscattered electron (BSE) images and quantitative elemental data were acquired using the CBS detector under operating conditions of 15.0 kV accelerating voltage, a beam current of 5.5 nA, and a working distance of $\sim$ 6.7 mm.

To further survey nanoscale features within selected regions of interest identified by SEM, infrared scattering-type scanning near-field optical microscopy (IR s-SNOM) was employed. This technique allows non-destructive characterization with spatial resolution beyond the diffraction limit, while simultaneously providing topographic and optical information. Atomic force microscopy (AFM) images and near-field optical images were acquired using a commercial IR s-SNOM system (Bruker nanoIR3s) operated in tapping mode. For near-field measurements, an IR beam was focused on the apex of a gold-coated AFM tip (160AC-GG, OPUS). Illumination at 931 cm^{-1} was provided by a CO_2 laser (Access Laser, L4SL-13CO2), while additional frequencies were generated using a tunable IR laser (Carmina, APE GmbH). The scattered near-field signals were collected by an off axis parabolic mirror and detected using a mercury cadmium telluride detector. To suppress background noise and extract the near-field signal from the lunar meteorite, we demodulated the detected signals at the second harmonic of the tip oscillation frequency.

Subsequently, transmission electron microscopy (TEM) was employed to characterize the crystal structures and nanoscale compositional variations within selected regions of interest. Electron transparent specimen suitable for TEM analyses was prepared using a dual-beam focused ion beam (FIB) SEM system (Helios 5 UX, Thermo Scientific). A protective platinum layer was first deposited on the target region, followed by focused ion beam milling with a 30 kV Ga ion beam to extract the region of interest. The specimen was then further thinned to a final thickness of less than 100 nm to ensure electron transparency. We used a TEM system (JEM-F200, JEOL, Japan) to acquire electron diffraction patterns for crystal structure characterization and conducted elemental analysis using TEM-EDS. To further resolve elemental distributions and iron oxidation states at higher spatial resolution, a scanning transmission electron microscopy (STEM) system (JEM-ARM300F, JEOL, Japan) was employed to perform electron energy-loss spectroscopy (EELS) analyses, enabling nanoscale elemental mapping, determination of Fe valence states, and quantification of atomic concentrations. The EELS spectra were acquired using a Gatan 1069 K3 receiver, with a dispersion of 0.9 eV/channel.

As a complementary technique to the above characterization methods, atom probe tomography (APT) was employed to achieve atomic-scale quantitative elemental analysis and three-dimensional compositional mapping. To prepare the tip-shaped specimen required for APT analysis, a thin specimen was first extracted from the region of interest using a 30 kV Ga ion beam and subsequently milled into a sharp nanotip using a low-energy 5 kV Ga ion beam in a FIB-SEM system. APT analyses were performed using a LEAP 4000X HR system (IMAGO, USA) on a reconstructed volume of approximately $76 \times 76 \times 456$ nm. The measurements were conducted in laser-pulsing mode with a pulse frequency of 200 kHz, a pulse energy of 60 pJ, a base pressure of 10^{-9} Pa, and an evaporation rate of approximately 1%.

3. Results

3.1. Distribution of np-Fe^0 in the Lunar Meteorite

The lunar meteorite NWA 4734 is an unbrecciated mare basalt that was ejected from the Moon by an impact event and collected in Northwest Africa (Connolly Jr et al., 2008; Y. Wang et al., 2012) (Figure 1a). The samples we investigated were extracted from the interior of NWA 4734, away from the meteorite surface, and prepared as an epoxy mount (Figure S1a in Supporting Information S1). Corresponding BSE images exhibit heterogeneous textures composed of multiple mineral phases (Figures S1b and S1c in Supporting Information S1). Based on the elemental distribution mapping using EDS analyses (Figure S2 in Supporting Information S1), we identified the presence of pyroxene, plagioclase, olivine, silica, K-feldspar, and Fe-Ti-Cr oxides, in agreement with previous studies (Y. Wang et al., 2012; A. Wang et al., 2004; Miyahara et al., 2013). The dominant minerals are pyroxene with a rough and fractured texture, and plagioclase with a smooth surface. At the boundary between these two minerals, Fe-Ti-Cr oxides are often observed. According to the atomic proportions obtained from SEM-EDS analysis (Figure 1b), these oxides are consistent with solid solutions composed of ilmenite ($FeTiO_3$), ulvöspinel (Fe_2TiO_4), chromite ($FeCr_2O_4$), and hercynite ($FeAl_2O_4$), which are common Fe-bearing oxides in the lunar materials (Ivanyuk et al., 2017).

To survey the presence and distributions of np-Fe^0, we employed IR s-SNOM, which provides spatial resolution down to a few tens of nanometers and contrast arising from the infrared optical conductivity of metallic iron relative to the insulating mineral background (Hillenbrand et al., 2025; Zhao et al., 2025). Using IR s-SNOM, we non-destructively acquired both AFM and near-field optical signals simultaneously, revealing surface morphology and subsurface np-Fe^0 distributions (Govyadinov et al., 2014) (Figures 1c and 1d). In the AFM topography, a pronounced height contrast is observed between the Fe-Ti-Cr oxides and plagioclase, which may result from their different hardness, producing a height difference after polishing. The s-SNOM image reveals

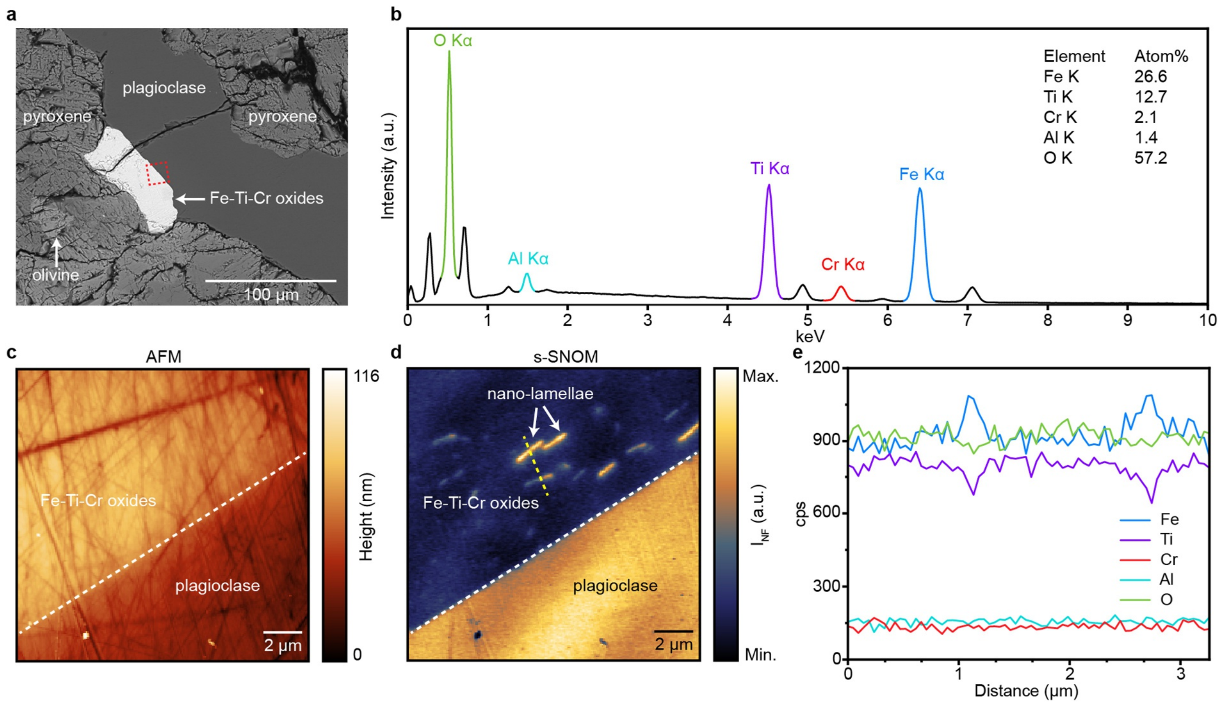

Figure 1. Np-Fe^0 in Fe-Ti-Cr oxides from the lunar meteorite NWA 4734. (a) BSE image showing a representative region of the lunar mare basalt meteorite. (b) SEM-EDS analysis of the Fe-Ti-Cr oxide region indicated in (a). (c) AFM topography image acquired at the boundary between Fe-Ti-Cr oxides and plagioclase, with the red dashed box in (a) indicating the measurement area. (d) Corresponding s-SNOM image recorded simultaneously at a laser frequency of 931 cm^{-1}. The yellow dashed line indicates the location of the SEM-EDS line scan shown in (e). (e) SEM-EDS line scan results showing elemental counts per second (cps) along the scan path.

distinct optical contrasts between the two minerals, thereby enabling clear identification, with the dark region corresponding to the solid solution and the bright region corresponding to plagioclase. In this representative Fe-Ti-Cr oxide grain, we observed numerous nanostructures that are not visible in the AFM topography, suggesting their subsurface location. By combining s-SNOM and SEM analyses, we confirmed that these nanostructures are exclusive to the Fe-Ti-Cr oxide solid solutions (Figures S3 and S4a in Supporting Information S1). A total of five Fe-Ti-Cr grains were investigated and all exhibit these nanostructures in similar density and distribution (Figures S4b–S4e in Supporting Information S1). The strong near-field signal of the nanostructures in s-SNOM reveals their high optical conductivity in the infrared spectral range, indicative of metallic behavior (Hillenbrand et al., 2025) (Figure S5 in Supporting Information S1). Subsequent SEM-EDS line scans reveal enhanced Fe signals at the nanostructure sites further supporting the possibility that they are composed of metallic iron (Figure 1e; Figure S6 in Supporting Information S1).

3.2. Morphology and Elemental Composition of np-Fe^0

We then selected representative nanostructures for FIB extraction to investigate their morphological characteristics and subsurface distribution, and to prepare specimens for subsequent APT and TEM measurements. The region marked by the grey shading in Figure 2a, which contains two relatively large nanostructures, was coated with a protective Pt layer prior to FIB extraction. The surrounding area outside the protective layer was then milled away, exposing the cross section of the designated solid solution region. As shown in Figure 2b, numerous nanostructures are present in the interior of the Fe-Ti-Cr oxide solid solution. Owing to their location deep inside the solid solution and their relatively small size, these features were not resolved in SEM imaging. After further thinning the sample to a thickness of approximately 50 nm, the cross-sectional view reveals that the two nanostructures appear as elongated features (Figure 2c), indicating that they possess continuous lamellar morphologies with nanometer-scale thicknesses and micrometer-scale lateral dimensions. This also demonstrates that the elongated features observed in the s-SNOM and SEM images originate from the nanometer-scale imaging depth, which exposes only near-surface sections of the lamellae.

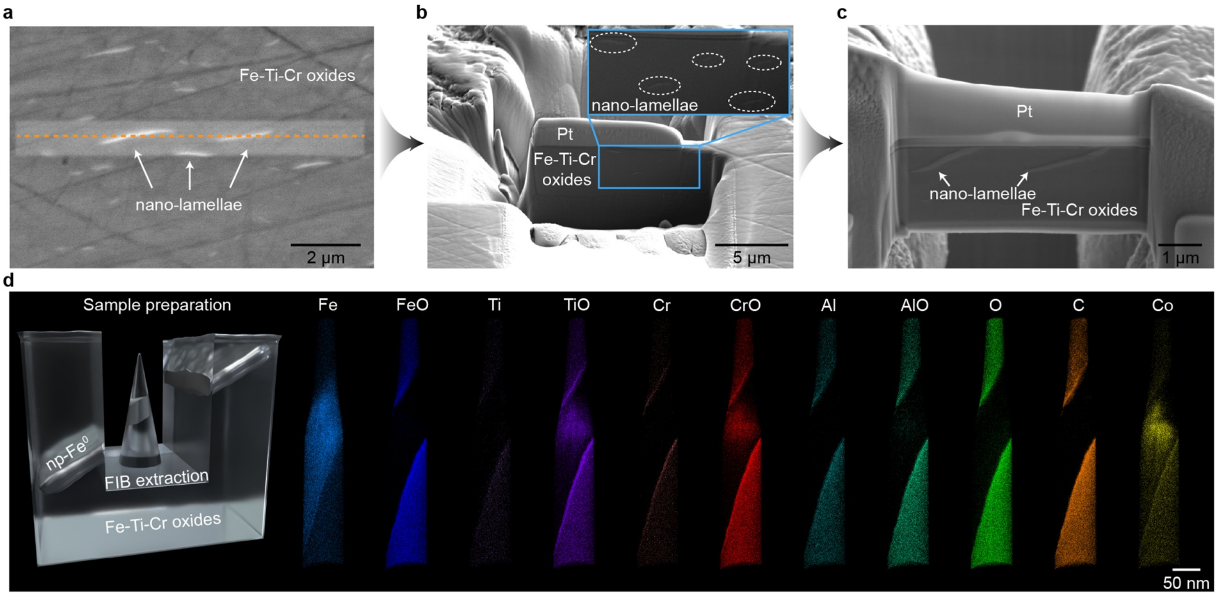

Figure 2. Lamellar morphology and three-dimensional elemental mapping of np-Fe^0. (a) BSE image of a Fe-Ti-Cr oxide solid solution region containing nanostructures. The grey rectangular shadow represents the region selected for FIB extraction, and the orange dashed line indicates the location of the final thin specimen shown in (c). (b) FIB cutting reveals numerous small nanostructures within the interior of the solid solution. The cyan boxed region is shown enlarged in the inset to highlight the nanostructures and their distribution. (c) Final thin specimen with a thickness of approximately 50 nm, showing the two selected representative nanostructures. (d) Schematic of APT tip-shaped specimen preparation and corresponding elemental composition analysis results. Scale bar: 50 nm.

To investigate the elemental composition and spatial distribution of the np-Fe^0 lamellae and the surrounding matrix, we performed APT for ultrahigh-resolution three-dimensional compositional analysis. A tip-shaped region including the nanostructure with dimensions of $456 \times 76 \times 76$ nm was analyzed (Figure 2d). The three-dimensional elemental maps reveal that in addition to the elements detected by SEM-EDS, trace amounts of C and Co are also identified by APT, both with concentrations below 0.6%. Regarding the elemental spatial distribution, Fe is concentrated within the nanostructure, whereas FeO is primarily detected in the surrounding matrix, indicating that the nanostructure is mainly composed of metallic iron. In contrast, Ti, Cr, and Al are predominantly present in the matrix, although signals of TiO, CrO, and AlO are also detected, suggesting the presence of their oxides inside this region. Additionally, C is primarily distributed in the matrix, while Co is preferentially enriched within the metallic core, probably due to its siderophilic behavior.

3.3. Three-Layer Core-Shell Structure

Quantitative analysis of structural and compositional variations within the lamellae, the surrounding matrix, and their interface is essential for a better understanding of the formation process of these nanostructures. To determine the crystal structure of the nanostructure, a representative lamellar feature was selected for detailed TEM characterization (Figure 3a). The TEM image reveals that the internal morphology within the lamellar feature is heterogeneous. Subsequently, fast Fourier transform (FFT) electron diffraction patterns were acquired from two distinct locations marked in Figure 3a. The results demonstrate that both sites exhibit the crystal structure of α-Fe. However, their relative crystallographic orientations differ, corresponding to the $[\bar{1}\,\bar{1}\,1]$ and [100] zone axes, respectively. This not only confirms the presence of elemental iron within the lamellar feature, but also demonstrates that the crystallographic orientation varies across different positions within a single lamellar feature, thereby indicating the polycrystalline nature of the lamellae. In addition, we also performed TEM-EDS analysis on both the np-Fe^0 core and several distant locations to examine variations in elemental composition (Figures S7a and S7b in Supporting Information S1), revealing elevated Fe content with residual O, indicative of partial oxidation within the core.

To further analyze the spatial distribution of metallic iron and Fe-bearing oxides, EELS measurements were conducted on the region containing the nanostructure using STEM. Based on the high-angle annular dark-field (HAADF) image and the multiple linear least-squares (MLLS) analysis (Cymes et al., 2023), three distinct

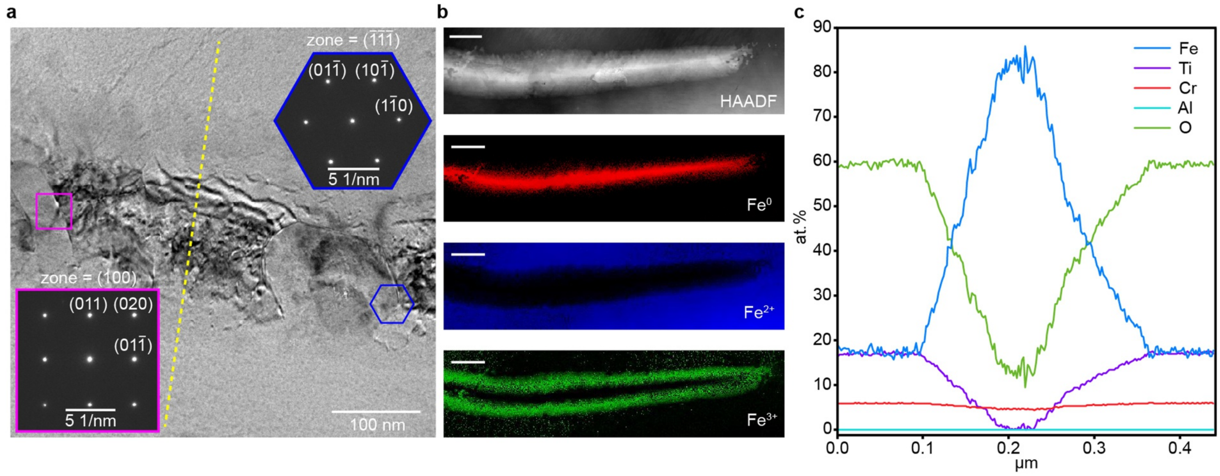

Figure 3. Quantitative analysis of the three-layer core-shell structure of np-Fe^0 lamellae. (a) TEM image of a region containing a nanostructure and its surrounding matrix, with FFT patterns obtained from two different locations. The yellow dashed line indicates the line scan path analyzed in (c). (b) STEM-HAADF image of the selected nanostructure and its surrounding matrix, along with corresponding EELS maps showing spatial distributions of Fe in three valence states. Scale bar: 200 nm. (c) EELS line scan profiles acquired along the yellow dashed line in (a), showing variations in elemental concentrations across the nanostructure.

valence states of Fe were identified (Figure 3b). The spatial distribution of these valence states form a three-layer core-shell structure in which metallic Fe^0 is concentrated in the nanostructure core, Fe^{3+} forms an adjacent shell, and Fe^{2+} is distributed in the surrounding matrix.

STEM-EELS measurements provide atomic-scale spatial resolution, enabling detailed analysis of compositional variations across the nanostructure (Figure 3c; Figure S7c in Supporting Information S1). The line scan profiles reveal that Fe accounts for ∼85% of the atoms in the nanostructure core, with ∼10% O indicating the presence of residual oxides. In the outer region, Fe and Ti concentrations are comparable, and the Fe-Ti-O ratios approximate those of ilmenite. However, the presence of Cr- and Al-bearing oxides consumes additional O, resulting in an actual O content lower than that required for pure ilmenite. Combined with an increase in Fe and concurrent decreases in Ti and O, these observations indicate the presence of ilmenite, a portion of which has undergone decomposition. Notably, quantitative analyses of atomic concentrations performed over the Fe-Ti-Cr oxide solid solution (Figure 1b) and point measurements at locations farther from the nanostructure (Figure S7b in Supporting Information S1) both show substantial deviations from the theoretical composition of ilmenite. This suggests that the relatively pure ilmenite adjacent to the nanostructure is either a residual phase retained following the reaction of other solid solution components, or a product of decomposition during phase separation.

4. Discussion

4.1. Observational Constraints on the Origin of np-Fe^0 Lamellae

Based on the experimental results, we aim to investigate the formation mechanisms of these np-Fe^0 lamellae based on three key observations. First, FIB cross-sectional imaging reveals that the lamellae are widely distributed within Fe-Ti-Cr oxide solid solutions and extend up to several micrometers in lateral dimensions (Figures 2a–2c). This large and continuous morphology differs from the typical np-Fe^0 particles formed by solar wind implantation or micrometeorite bombardment in lunar regolith. Similar high-resolution TEM studies (Chen et al., 2025; Li et al., 2022, 2025; Shen et al., 2024; Zeng et al., 2025) showed that impact events such as micrometeorite bombardment generally produce typical np-Fe^0 particles that occur near impact craters (Figure S8a in Supporting Information S1). By comparison, solar wind irradiation typically generates isolated grains confined within space-weathered amorphous rims (Figure S8b in Supporting Information S1). In contrast, the iron structures observed in this work are of elongated lamellar form rather than isolated particles, and are embedded throughout the interior of Fe-Ti-Cr oxide solid solutions (Figure S8c in Supporting Information S1), resembling subsolidus phase separation (Ivanyuk et al., 2017). Given that NWA 4734 experienced an impact event, as indicated by the presence of fractured pyroxene, olivine phenocrysts, and shock melt veins (Y. Wang et al., 2012), we suggest that the meteorite was subjected to high temperatures and pressures. The SEM and s-SNOM images presented above also reveal that the np-Fe^0 lamellae exhibit locally ordered orientations, which may be associated with the internal stress field generated during the impact event (Lyons et al., 1993). Moreover, the Ar-Ar age of NWA 4734 is younger than its crystallization age, further suggesting that the meteorite underwent shock-induced metamorphism (Chen et al., 2018; Fernandes et al., 2009). Therefore, we infer that the np-Fe^0 lamellae formed under the extreme thermal and mechanical conditions through reduction occurring during or shortly after an impact event within Fe-Ti-Cr oxide solid solutions crystallized from the melt.

Second, atomic proportions from EDS and EELS show that Fe-Ti-Cr oxide solid solutions in NWA 4734 are not simple ilmenite. In addition to ilmenite, the composition of the matrix indicates solid solutions involving other Fe-bearing oxides such as ulvöspinel and chromite. Previous line scans revealed ilmenite adjacent to the nanostructures, along with signs of partial decomposition. This may be explained by the following reduction pathway. Fe^{2+} in ulvöspinel is more easily reduced than that in ilmenite (O'Neill et al., 1988), resulting in preferential formation of np-Fe^0 from ulvöspinel, while ilmenite remains comparatively unaltered. Ilmenite is one of the products formed through redox reactions of ulvöspinel, further contributing to its enrichment in the matrix surrounding the nanostructures. With continued reduction, ilmenite also undergoes decomposition.

Third, besides the Fe-Ti-Cr oxide solid solutions, we also identified regions characterized by Fe-Ti oxide solid solutions (Figure S9 in Supporting Information S1). However, no np-Fe^0 lamellae were observed within the Fe-Ti oxide regions. This finding suggests that the presence of Cr may play a critical role in promoting the formation of np-Fe^0. The incorporation of Cr may modify the lattice properties of Fe-Ti-Cr oxides relative to Fe-Ti oxides, making them more susceptible to reduction reactions under space weathering such as cosmic ray irradiation (Chen et al., 2024; McKay et al., 1991; Pieters & Noble, 2016). Additionally, Cr may participate in the reduction of Fe^{2+} and Fe^{3+}, either directly or by acting as a catalyst that facilitates electron transfer in redox processes (Schreiber et al., 1982).

4.2. Shock-Induced Reduction and Disproportionation Mechanisms

Building on the three observations described above, we hypothesize that np-Fe^0 lamellae formed within Fe-Ti-Cr oxide solid solutions through the following processes (Figure 4). During or shortly after the impact event, NWA 4734 likely experienced high-temperature and high-pressure conditions, as reported in previous studies (Connolly Jr et al., 2008; Y. Wang et al., 2012). Experimental and modeling studies have estimated the bulk shock pressure of this meteorite to 20–30 GPa (Ray et al., 2024; Xie et al., 2025), and locally even higher as implied by heterogeneous distribution of mineral grains (Y. Wang et al., 2012). The presence of these np-Fe^0 lamellae within the Fe-Ti-Cr oxides effectively constrains the shock-induced temperature conditions. Thermodynamically, subsolidus thermal decomposition and the subsequent exsolution of metallic iron within the similar ulvöspinel–ilmenite–iron system are activated specifically within the 1123–1483 K temperature range (Taylor et al., 1972). This experimental threshold aligns well with the thermal excursions exceeding 1000 K estimated from other coexisting metamorphic minerals in the sample (Chen et al., 2018; O'Neill et al., 1988). Consequently, the distinct occurrence of these lamellae indicates that local shock-induced thermal excursions successfully reached the high-temperature conditions required for the reduction to metallic iron.

Such impact-generated environments are known to be highly reducing, consistent with the redox conditions produced during large-scale impact events (Gu et al., 2025; Pang et al., 2024). Under these shock-induced reducing conditions, Fe-Ti-Cr oxide solid solutions containing ulvöspinel and ilmenite components become thermodynamically susceptible to reduction. This enhanced instability originates from the elevated equilibrium oxygen fugacity of the ulvöspinel-ilmenite-iron buffer at higher temperatures, which destabilizes Fe-rich spinel and promotes its decomposition (O'Neill et al., 1988). Meanwhile, the release and outward diffusion of oxygen establish an oxygen potential gradient that further drives the progression of the decomposition reaction (Pang et al., 2024). This thermodynamic behavior aligns with our observations that Ti/Cr-rich spinel coexists with np-Fe^0, in agreement with theoretical predictions that reduction-precipitation occurs in Fe_3O_4-Fe_2TiO_4-type solid solutions at high temperature and low oxygen fugacity (O'Neill et al., 1988). On the basis of these thermodynamic constraints and redox observations, the ulvöspinel and ilmenite components could undergo the following reduction reactions:

$$2Fe_2TiO_4 \rightarrow 2Fe + O_2 + 2FeTiO_3 \quad (1)$$

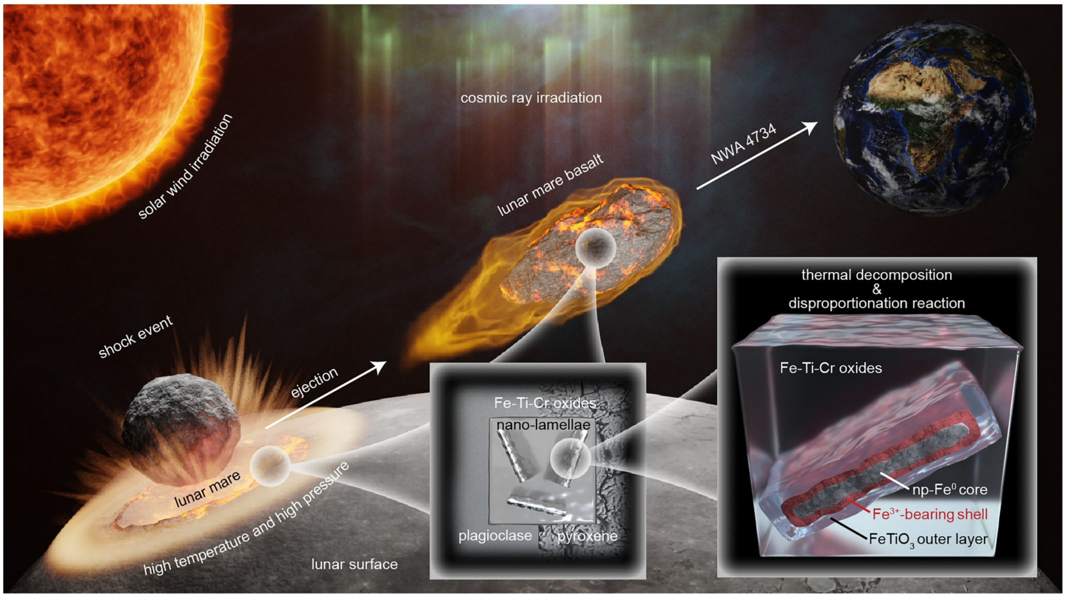

Figure 4. Schematic of the proposed formation mechanism of the np-Fe^0 lamellae. Large-scale impact event on the lunar surface generates extreme temperature and pressure conditions, resulting in significant shock metamorphic features including melt veins and pervasive fractured morphologies within the host mare basalt. Under these extreme conditions, np-Fe^0 lamellae precipitate within the Fe-Ti-Cr oxide solid solutions through thermal decomposition and disproportionation reactions. These lamellae exhibit a distinctive three-layer core-shell structure characterized by a metallic Fe^0 core, an Fe^{3+}-bearing intermediate shell, and an ilmenite-dominated outer layer. Portions of these shocked basaltic materials, bearing the np-Fe^0 lamellae, were ejected from the lunar surface and eventually delivered to Earth as the NWA 4734 meteorite.

$$2FeTiO_3 \rightarrow 2Fe + O_2 + 2TiO_2 \quad (2)$$

As a result, Fe^{2+} is progressively reduced and precipitates as metallic iron, while the residual phase evolves toward Ti- and Cr-enriched endmembers. The reduced metallic iron nucleates in situ, and its growth is constrained by the confined local environment and restricted long-range diffusion during the rapid cooling (Khisina et al., 2013; Meldrum & O'Shaughnessy, 2020; Theriault & Fowler, 1995). These kinetic restrictions promote the development of anisotropic aggregates, leading to elongated metallic nanodomains and producing the observed nano-lamellar morphology.

We further examine the formation process of this three-layer core-shell structure. The extreme pressure, temperature gradients, and abundant defects generated during the impact event drive redox reactions within the Fe-Ti solid solution, rendering Fe^{2+} thermodynamically unstable (Khisina et al., 2013; O'Neill et al., 1988; Qin et al., 2025). As the reaction proceeds, oxygen released during high-temperature pyrolysis (Allen et al., 1996) can promote rapid oxidation in the outer regions of the developing nanodomains, producing Fe^{3+}-bearing phases at their margins. Following the shock, the heat generated by the impact is rapidly dissipated into the surrounding vacuum, and the subsequent quenching abruptly halts further reaction evolution (Ahrens & O'Keefe, 1972; Cintala, 1992; Fritz et al., 2005). This non-equilibrium cooling preserves the partial reaction products and stabilizes the compositional gradients established during reduction and localized oxidation (Anand et al., 2006; Hu & Sharp, 2022). Consequently, the nanostructures develop into a three-layer structure consisting of an outer layer enriched in ilmenite, a transition zone containing Fe^{3+}, and an inner core composed predominantly of metallic iron. Considering both the reduction and oxidation processes, the overall transformation can be represented by disproportionation reactions such as:

$$3Fe_2TiO_4 \rightarrow Fe + Fe_2O_3 + 3FeTiO_3 \quad (3)$$

$$3FeTiO_3 \rightarrow Fe + Fe_2O_3 + 3TiO_2 \quad (4)$$

These reactions may also proceed directly under shock-induced high-pressure conditions, which are known to strongly enhance disproportionation pathways (Bindi et al., 2020; Li et al., 2022). In addition, metallic iron produced via disproportionation has been extensively documented in Earth's deep mantle minerals (Pan et al., 2025; Zhang et al., 2014). These terrestrial studies demonstrate that extreme temperature and pressure conditions can render Fe^{2+} thermodynamically unstable, triggering redox reactions that lead to the generation of metallic iron. This internal planetary process provides another possible mechanism for the formation of the observed nanostructures. However, it is worth noting that metallic iron generated under such quasi-steady-state conditions over extended geological timescales typically exhibits a spherical morphology, rather than the lamellar morphology observed here, due to free energy minimization (Butler & Banerjee, 1975; Thompson et al., 2017; Xiong et al., 2024).

Notably, the np-Fe^0 identified in this study reveals a potentially significant component of impact-generated iron within the Moon, contributing to the global iron content of the Moon (Gu et al., 2025). In contrast to the Apollo and Chang'e returned lunar samples, lunar meteorites experience the large-scale impact events required to eject material from the lunar surface. Such shock conditions facilitate the formation of the lamellar metallic iron textures described here, which are absent in returned samples. Unlike the weathering-derived np-Fe^0 that forms in varieties such as surface coatings on regolith grains (Escobar-Cerezo et al., 2018; Hapke, 2001; Wu & Hapke, 2018), the internally hosted metallic iron documented in this study exerts an endogenic influence on spectral behavior (Britt & Pieters, 1994; Zhang & Cloutis, 2021). Iron inclusions enclosed within mineral grains may represent a fundamental mineralogical source of local spectral heterogeneity (Clark & Roush, 1984; Robinson et al., 2008; Zou et al., 2004), including the spectral contrasts commonly observed between mare and highland terrains. These findings provide an important basis for the precise interpretation of lunar remote-sensing spectra.

5. Conclusions

In conclusion, we identified np-Fe^0 lamellae within the interior of the lunar meteorite NWA 4734, which exhibit a continuous lamellar morphology and a distinctive three-layer core-shell structure. Our microscopic and quantitative analyses reveal Fe-Ti-Cr oxide solid solutions in the lunar meteorite and provide evidence of redox reactions induced by extreme conditions and complex geological processes during the impact event. This structure not only preserves a record of the non-equilibrium evolution pathway of lunar minerals during an instantaneous shock event, but also reveals an iron formation mechanism distinct from that driven by space weathering. Moreover, the formation of np-Fe^0 appears to be strongly influenced by the mineralogy composition of the solid solutions. We believe that similar phenomena may arise in comparable systems under suitable environments, extending beyond lunar materials. These findings deepen our knowledge of the microscopic reaction processes in lunar materials, provide new perspectives on the geological evolution of the Moon, and open new avenues for the artificial fabrication of metallic iron nanostructures with potential applications in materials science and space exploration.

Conflict of Interest

The authors declare no conflicts of interest relevant to this study.

Availability Statement

The original data sets are available in the Mendeley repository (Zhou, 2026).

Acknowledgments
This research has been supported by the National Natural Science Foundation of China (42277156, 42221002, 62175188, 62475194), the National Key R&D Program of China (2024YFB2808100), the Science and Technology Commission of Shanghai Municipality (23ZR1465800, 23190712300), Fundamental Research Funds for the Central Universities, Start-up Research Fund of University of Science and Technology of China (KY2110000057) and NSF Science and Technology Center on Real-Time Functional Imaging (STROBE) (DMR-1548924). The authors thank the staff of Scientific Compass (www.shiyanjia.com) for their support with the SEM and TEM experiments. The authors thank Prof. Xinbin Cheng for his valuable discussions.

References

Ahrens, T. J., & O'Keefe, J. D. (1972). Shock melting and vaporization of lunar rocks and minerals. *The moon*, *4*(1), 214–249. https://doi.org/10.1007/bf00562927

Allen, C., Morris, R., Lauer Jr., H., & McKay, D. (1993). Microscopic iron metal on glass and minerals—A tool for studying regolith maturity. *Icarus*, *104*(2), 291–300. https://doi.org/10.1006/icar.1993.1102

Allen, C. C., Morris, R. V., & McKay, D. S. (1996). Oxygen extraction from lunar soils and pyroclastic glass. *Journal of Geophysical Research*, *101*(E11), 26085–26095. https://doi.org/10.1029/96je02726

Anand, M., Taylor, L. A., Floss, C., Neal, C. R., Terada, K., & Tanikawa, S. (2006). Petrology and geochemistry of LaPaz Icefield 02205: A new unique low-Ti mare-basalt meteorite. *Geochimica et Cosmochimica Acta*, *70*(1), 246–264. https://doi.org/10.1016/j.gca.2005.08.018

Anand, M., Taylor, L. A., Nazarov, M. A., Shu, J., Mao, H.-K., & Hemley, R. J. (2004). Space weathering on airless planetary bodies: Clues from the lunar mineral hapkeite. *Proceedings of the National Academy of Sciences*, *101*(18), 6847–6851. https://doi.org/10.1073/pnas.0401565101

Beard, B. L., & Johnson, C. M. (2004). Fe isotope variations in the modern and ancient Earth and other planetary bodies. *Reviews in Mineralogy and Geochemistry*, *55*(1), 319–357. https://doi.org/10.2138/gsrmg.55.1.319

Bindi, L., Shim, S.-H., Sharp, T. G., & Xie, X. (2020). Evidence for the charge disproportionation of iron in extraterrestrial bridgmanite. *Science Advances*, *6*(2), eaay7893. https://doi.org/10.1126/sciadv.aay7893

Britt, D., & Pieters, C. (1994). Darkening in black and gas-rich ordinary chondrites: The spectral effects of opaque morphology and distribution. *Geochimica et Cosmochimica Acta*, *58*(18), 3905–3919. https://doi.org/10.1016/0016-7037(94)90370-0

Butler, R. F., & Banerjee, S. K. (1975). Single-domain grain size limits for metallic iron. *Journal of Geophysical Research*, *80*(2), 252–259. https://doi.org/10.1029/jb080i002p00252

Cao, Z., Guo, Z., Li, C., Zhao, S., Li, Y., He, Q., et al. (2024). Submicroscopic magnetite may be ubiquitous in the lunar regolith of the high-Ti region. *Science Advances*, *10*(38), eadn2301. https://doi.org/10.1126/sciadv.adn2301

Chen, J., Wang, A., Jolliff, B., Korotev, R., Ling, Z., Fu, X., & Ni, Y. (2018). Petrogenetic and shock history of mare basaltic lunar meteorite Northwest Africa 4734. In *49th Annual Lunar and Planetary Science Conference*.2976.

Chen, X., Yang, S., Chen, G., Xu, W., Song, L., Li, A., et al. (2024). Massive water production from lunar ilmenite through reaction with endogenous hydrogen. *The Innovation*, *5*, 100690. https://doi.org/10.1016/j.xinn.2024.100690

Chen, Y., Cao, Z., Li, C., Li, Y., Han, Z., Wang, X., et al. (2025). Characteristics of weak space weathering in Chang'e-5 lunar soil: Evidence from microcraters formed by low-speed impacts. *Journal of Geophysical Research: Planets*, *130*(10), e2025JE009293. https://doi.org/10.1029/2025je009293

Cintala, M. J. (1992). Impact-induced thermal effects in the lunar and mercurian regoliths. *Journal of Geophysical Research*, *97*(E1), 947–973. https://doi.org/10.1029/91je02207

Clark, R. N., & Roush, T. L. (1984). Reflectance spectroscopy: Quantitative analysis techniques for remote sensing applications. *Journal of Geophysical Research*, *89*(B7), 6329–6340. https://doi.org/10.1029/jb089ib07p06329

Comstock, G. (1977). On deciphering the particle track record of lunar regolith history. *Journal of Geophysical Research*, *82*(2), 357–367. https://doi.org/10.1029/jb082i002p00357

Connolly Jr., H. C., Smith, C., Benedix, G., Folco, L., Righter, K., Zipfel, J., et al. (2008). The meteoritical bulletin, no. 93, 2008 March. *Meteoritics & Planetary Science*, *43*(3), 571–632. https://doi.org/10.1111/j.1945-5100.2008.tb00673.x

Cymes, B. A., Burgess, K. D., & Stroud, R. M. (2023). Detection of ferric iron in an exsolved lunar pyroxene using electron energy loss spectroscopy (EELS): Implications for space weathering and redox conditions on the moon. *Meteoritics & Planetary Science*, *58*(2), 259–274. https://doi.org/10.1111/maps.13941

DellaGiustina, D. N., Burke, K., Walsh, K. J., Smith, P. H., Golish, D. R., Bierhaus, E. B., et al. (2020). Variations in color and reflectance on the surface of asteroid (101955) Bennu. *Science*, *370*(6517), eabc3660. https://doi.org/10.1126/science.abc3660

Denevi, B. W., Noble, S. K., Christoffersen, R., Thompson, M. S., Glotch, T. D., Blewett, D. T., et al. (2023). Space weathering at the Moon. *Reviews in Mineralogy and Geochemistry*, *89*(1), 611–650. https://doi.org/10.2138/rmg.2023.89.14

Escobar-Cerezo, J., Penttilä, A., Kohout, T., Muñoz, O., Moreno, F., & Muinonen, K. (2018). Simulations of effects of nanophase iron space weather products on lunar regolith reflectance spectra. *The Astrophysical Journal*, *853*(1), 71. https://doi.org/10.3847/1538-4357/aaa24d

Fernandes, V., Korotev, R., & Renne, P. (2009). ^{40}Ar-^{39}Ar ages and chemical composition for lunar mare basalts: NWA 4734 and NWA 4898. In *40th Annual Lunar and Planetary Science Conference*.1045.

Fritz, J., Artemieva, N., & Greshake, A. (2005). Ejection of Martian meteorites. *Meteoritics & Planetary Science*, *40*(9–10), 1393–1411. https://doi.org/10.1111/j.1945-5100.2005.tb00409.x

Frost, D. J., Liebske, C., Langenhorst, F., McCammon, C. A., Trønnes, R. G., & Rubie, D. C. (2004). Experimental evidence for the existence of iron-rich metal in the Earth's lower mantle. *Nature*, *428*(6981), 409–412. https://doi.org/10.1038/nature02413

Gopon, P., Spicuzza, M. J., Kelly, T. F., Reinhard, D., Prosa, T. J., & Fournelle, J. (2017). Ultra-reduced phases in Apollo 16 regolith: Combined field emission electron probe microanalysis and atom probe tomography of submicron Fe-Si grains in Apollo 16 sample 61500. *Meteoritics & Planetary Science*, *52*(9), 1941–1962. https://doi.org/10.1111/maps.12899

Govyadinov, A. A., Mastel, S., Golmar, F., Chuvilin, A., Carney, P. S., & Hillenbrand, R. (2014). Recovery of permittivity and depth from near-field data as a step toward infrared nanotomography. *ACS Nano*, *8*(7), 6911–6921. https://doi.org/10.1021/nn5016314

Gu, L., Wang, N., Lin, Y., Tian, H., Tang, X., Zhou, Z., et al. (2025). Abundant high-pressure minerals and submicroscopic metallic iron discovered in a shocked lunar meteorite. *Communications Earth & Environment*, *6*(1), 915. https://doi.org/10.1038/s43247-025-02876-z

Guo, J.-G., Ying, T., Gao, H., Chen, X., Song, Y., Lin, T., et al. (2022). Surface microstructures of lunar soil returned by Chang'e-5 mission reveal an intermediate stage in space weathering process. *Science Bulletin*, *67*(16), 1696–1701. https://doi.org/10.1016/j.scib.2022.06.019

Guo, Z., Li, C., Li, Y., Wen, Y., Tai, K., Li, X., et al. (2022). Nanophase iron particles derived from fayalitic olivine decomposition in Chang'e-5 lunar soil: Implications for thermal effects during impacts. *Geophysical Research Letters*, *49*(5), e2021GL097323. https://doi.org/10.1029/2021gl097323

Hapke, B. (2001). Space weathering from Mercury to the asteroid belt. *Journal of Geophysical Research*, *106*(E5), 10039–10073. https://doi.org/10.1029/2000je001338

Hillenbrand, R., Abate, Y., Liu, M., Chen, X., & Basov, D. N. (2025). Visible-to-THz near-field nanoscopy. *Nature Reviews Materials*, *10*(4), 285–310. https://doi.org/10.1038/s41578-024-00761-3

Hu, J., & Sharp, T. G. (2022). Formation, preservation and extinction of high-pressure minerals in meteorites: Temperature effects in shock metamorphism and shock classification. *Progress in Earth and Planetary Science*, *9*(1), 6. https://doi.org/10.1186/s40645-021-00463-2

Ivanyuk, G. Y., Kalashnikov, A. O., Pakhomovsky, Y. A., Bazai, A. V., Goryainov, P. M., Mikhailova, J. A., et al. (2017). Subsolidus evolution of the magnetite-spinel-ulvöspinel solid solutions in the Kovdor phoscorite-carbonatite complex, NW Russia. *Minerals*, *7*(11), 215. https://doi.org/10.3390/min7110215

Johnson, C. M., Beard, B. L., & Roden, E. E. (2008). The iron isotope fingerprints of redox and biogeochemical cycling in modern and ancient Earth. *Annual Review of Earth and Planetary Sciences*, *36*(1), 457–493. https://doi.org/10.1146/annurev.earth.36.031207.124139

Keller, L. P., Berger, E. L., Zhang, S., & Christoffersen, R. (2021). Solar energetic particle tracks in lunar samples: A transmission electron microscope calibration and implications for lunar space weathering. *Meteoritics & Planetary Science*, *56*(9), 1685–1707. https://doi.org/10.1111/maps.13732

Keller, L. P., & McKay, D. S. (1993). Discovery of vapor deposits in the lunar regolith. *Science*, *261*(5126), 1305–1307. https://doi.org/10.1126/science.261.5126.1305

Keller, L. P., & McKay, D. S. (1997). The nature and origin of rims on lunar soil grains. *Geochimica et Cosmochimica Acta*, *61*(11), 2331–2341. https://doi.org/10.1016/s0016-7037(97)00085-9

Khisina, N., Wirth, R., Abart, R., Rhede, D., & Heinrich, W. (2013). Oriented chromite–diopside symplectic inclusions in olivine from lunar regolith delivered by "Luna-24" mission. *Geochimica et Cosmochimica Acta*, *104*, 84–98. https://doi.org/10.1016/j.gca.2012.10.050

Li, C., Guo, Z., Li, Y., Tai, K., Wei, K., Li, X., et al. (2022). Impact-driven disproportionation origin of nanophase iron particles in Chang'e-5 lunar soil sample. *Nature Astronomy*, *6*(10), 1156–1162. https://doi.org/10.1038/s41550-022-01763-3

Li, C., Li, Y., Pang, R., Xie, J., Han, Z., Wen, Y., et al. (2025). Impact-induced ultra-high melting point oldhamite discovered in Chang'e-6 lunar soil. *Nature Communications*, *16*(1), 2155. https://doi.org/10.1038/s41467-025-57337-0

Liu, Y., Cao, H., Li, R., Chen, J., Yin, C., Jia, Z., et al. (2025). Discovery of crystalline Fe_2O_3 in returned lunar soils. *Science Advances*, *11*(46), eady5169. https://doi.org/10.1126/sciadv.ady5169

Lu, X., Chen, J., Ling, Z., Liu, C., Fu, X., Qiao, L., et al. (2023). Mature lunar soils from Fe-rich and young mare basalts in the Chang'e-5 regolith samples. *Nature Astronomy*, *7*, 142–151.

Lyons, J. B., Officer, C. B., Borella, P. E., & Lahodynsky, R. (1993). Planar lamellar substructures in quartz. *Earth and Planetary Science Letters*, *119*(3), 431–440. https://doi.org/10.1016/0012-821x(93)90151-x

Mandt, K. E. (2024). The scientific importance of the lunar environment. *Science*, *384*(6692), eado9563. https://doi.org/10.1126/science.ado9563

Maurette, M., & Price, P. B. (1975). Electron microscopy of irradiation effects in space. *Science*, *187*(4172), 121–129. https://doi.org/10.1126/science.187.4172.121

McKay, D. S., Heiken, G., Basu, A., Blanford, G., Simon, S., Reedy, R., et al. (1991). The lunar regolith. *Lunar sourcebook*, *567*, 285–356.

Meldrum, F. C., & O'Shaughnessy, C. (2020). Crystallization in confinement. *Advanced Materials*, *32*(31), 2001068. https://doi.org/10.1002/adma.202001068

Miyahara, M., Kaneko, S., Ohtani, E., Sakai, T., Nagase, T., Kayama, M., et al. (2013). Discovery of seifertite in a shocked lunar meteorite. *Nature Communications*, *4*(1), 1737. https://doi.org/10.1038/ncomms2733

Noguchi, T., Nakamura, T., Kimura, M., Zolensky, M. E., Tanaka, M., Hashimoto, T., et al. (2011). Incipient space weathering observed on the surface of Itokawa dust particles. *Science*, *333*(6046), 1121–1125. https://doi.org/10.1126/science.1207794

O'Neill, H. S. C., Pownceby, M. I., & Wall, V. J. (1988). Ilmenite-rutile-iron and ulvospinel-ilmenite-iron equilibria and the thermochemistry of ilmenite ($FeTiO_3$) and ulvospinel (Fe_2TiO_4). *Geochimica et Cosmochimica Acta*, *52*(8), 2065–2072. https://doi.org/10.1016/0016-7037(88)90185-8

Pan, F., Wu, X., Wang, C., Zhang, Y., Yang, Y., He, X., et al. (2025). Iron disproportionation in peridotite fragments from the mantle transition zone. *Nature Communications*, *16*(1), 5440. https://doi.org/10.1038/s41467-025-60566-y

Pang, R., Yang, J., Li, R., Liu, S., Li, Q., Zhu, D., et al. (2024). Redox condition changes caused by impacts: Insights from Chang'e-5 lunar glass beads. *Science Bulletin*, *69*(10), 1495–1505. https://doi.org/10.1016/j.scib.2024.03.004

Pieters, C. M., Ammannito, E., Blewett, D. T., Denevi, B. W., De Sanctis, M. C., Gaffey, M. J., et al. (2012). Distinctive space weathering on Vesta from regolith mixing processes. *Nature*, *491*(7422), 79–82. https://doi.org/10.1038/nature11534

Pieters, C. M., & Noble, S. K. (2016). Space weathering on airless bodies. *Journal of Geophysical Research: Planets*, *121*(10), 1865–1884. https://doi.org/10.1002/2016je005128

Qin, Z., Li, Y., Li, C., Pang, R., Wen, Y., Li, R., et al. (2025). Minimum measured temperature at which np-Fe^0 forms in ilmenite of lunar soil: Evidence from in-situ TEM heating experiments. *Acta Geochimica*, *45*, 1–10. https://doi.org/10.1007/s11631-025-00831-5

Ray, D., Misra, S., Park, C., Newsom, H. E., & Peterson, E. J. (2024). Maskelynite-as seen in shocked Lonar target basalt, India, and martian and lunar meteorites. *Geochemistry*, *84*(2), 126127. https://doi.org/10.1016/j.chemer.2024.126127

Robinson, M. S., Murchie, S. L., Blewett, D. T., Domingue, D. L., Hawkins, S. E., Head, J. W., et al. (2008). Reflectance and color variations on mercury: Regolith processes and compositional heterogeneity. *Science*, *321*(5885), 66–69. https://doi.org/10.1126/science.1160080

Sasaki, S., Nakamura, K., Hamabe, Y., Kurahashi, E., & Hiroi, T. (2001). Production of iron nanoparticles by laser irradiation in a simulation of lunar-like space weathering. *Nature*, *410*(6828), 555–557. https://doi.org/10.1038/35069013

Schreiber, H. D., Balazs, G. B., Shaffer, A. P., & Jamison, P. L. (1982). Iron metal production in silicate melts through the direct reduction of Fe (ii) by Ti (iii), Cr (ii), and Eu (ii). *Geochimica et Cosmochimica Acta*, *46*(10), 1891–1901. https://doi.org/10.1016/0016-7037(82)90127-2

Shen, L., Zhao, R., Chang, C., Yu, J., Xiao, D., Bai, H., et al. (2024). Separate effects of irradiation and impacts on lunar metallic iron formation observed in Chang'e-5 samples. *Nature Astronomy*, *8*(9), 1110–1118. https://doi.org/10.1038/s41550-024-02300-0

Taylor, K. G., & Konhauser, K. O. (2011). Iron in earth surface systems: A major player in chemical and biological processes. *Elements*, *7*(2), 83–88. https://doi.org/10.2113/gselements.7.2.83

Taylor, L. A., Pieters, C. M., Keller, L. P., Morris, R. V., & McKay, D. S. (2001). Lunar mare soils: Space weathering and the major effects of surface-correlated nanophase Fe. *Journal of Geophysical Research*, *106*(E11), 27985–27999. https://doi.org/10.1029/2000je001402

Taylor, L. A., Williams, R. J., & McCallister, R. H. (1972). Stability relations of ilmenite and ulvöspinel in the Fe-Ti-O system and application of these data to lunar mineral assemblages. *Earth and Planetary Science Letters*, *16*(2), 282–288. https://doi.org/10.1016/0012-821x(72)90204-x

Theriault, R., & Fowler, A. (1995). Harrisitic textures in the centre hill complex, munro township, Ontario: Product of diffusion limited growth. *Mineralogy and Petrology*, *54*(1), 35–44.

Thompson, M. S., Zega, T. J., Becerra, P., Keane, J. T., & Byrne, S. (2016). The oxidation state of nanophase Fe particles in lunar soil: Implications for space weathering. *Meteoritics & Planetary Science*, *51*(6), 1082–1095. https://doi.org/10.1111/maps.12646

Thompson, M. S., Zega, T. J., & Howe, J. Y. (2017). In situ experimental formation and growth of Fe nanoparticles and vesicles in lunar soil. *Meteoritics & Planetary Science*, *52*(3), 413–427. https://doi.org/10.1111/maps.12798

Wang, A., Kuebler, K. E., Jolliff, B. L., & Haskin, L. A. (2004). Raman spectroscopy of Fe-Ti-Cr-oxides, case study: Martian meteorite EETA79001. *American Mineralogist*, *89*(5–6), 665–680. https://doi.org/10.2138/am-2004-5-601

Wang, K., Moynier, F., Podosek, F. A., & Foriel, J. (2012). An iron isotope perspective on the origin of the nanophase metallic iron in lunar regolith. *Earth and Planetary Science Letters*, *337*, 17–24. https://doi.org/10.1016/j.epsl.2012.05.021

Wang, Y., Hsu, W., Guan, Y., Li, X., Li, Q., Liu, Y., & Tang, G. (2012). Petrogenesis of the Northwest Africa 4734 basaltic lunar meteorite. *Geochimica et Cosmochimica Acta*, *92*, 329–344. https://doi.org/10.1016/j.gca.2012.06.024

Warren, P. H., Jerde, E. A., & Kallemeyn, G. W. (1989). Lunar meteorites: Siderophile element contents, and implications for the composition and origin of the Moon. *Earth and Planetary Science Letters*, *91*(3–4), 245–260. https://doi.org/10.1016/0012-821x(89)90001-0

Weber, I., Stojic, A. N., Morlok, A., Reitze, M. P., Markus, K., Hiesinger, H., et al. (2020). Space weathering by simulated micrometeorite bombardment on natural olivine and pyroxene: A coordinated IR and TEM study. *Earth and Planetary Science Letters*, *530*, 115884. https://doi.org/10.1016/j.epsl.2019.115884

Wu, Y., & Hapke, B. (2018). Spectroscopic observations of the Moon at the lunar surface. *Earth and Planetary Science Letters*, *484*, 145–153. https://doi.org/10.1016/j.epsl.2017.12.003

Xian, H., Zhu, J., Yang, Y., Li, S., Lin, X., Xi, J., et al. (2023). Ubiquitous and progressively increasing ferric iron content on the lunar surfaces revealed by the Chang'e-5 sample. *Nature Astronomy*, *7*(3), 280–286. https://doi.org/10.1038/s41550-022-01855-0

Xie, T., Shieh, S. R., Chariton, S., van Zyl, M., Rodriguez, R. D., Prakapenka, V. B., & Zhang, D. (2025). Plagioclase under compression: A path to diaplectic glass and maskelynite. *Science Advances*, *11*(25), eadv8231. https://doi.org/10.1126/sciadv.adv8231

Xiong, M., Wu, Y., Yao, W., Chen, Z., Yu, Y., Li, X., et al. (2024). The formation mechanisms of np-Fe in lunar regolith: A review. *Materials*, *17*(23), 5866. https://doi.org/10.3390/ma17235866

Zeng, X., Zhang, X., Wu, Y., Yu, W., Li, X., & Liu, J. (2025). Exotic nanophase iron as a new agent for space weathering on the Moon. *The Astrophysical Journal Letters*, *983*(1), L5. https://doi.org/10.3847/2041-8213/adbf88

Zhang, L., Meng, Y., Yang, W., Wang, L., Mao, W. L., Zeng, Q.-S., et al. (2014). Disproportionation of (Mg, Fe) SiO_3 perovskite in Earth's deep lower mantle. *Science*, *344*(6186), 877–882. https://doi.org/10.1126/science.1250274

Zhang, X., & Cloutis, E. (2021). Near-infrared spectra of lunar ferrous mineral mixtures. *Earth and Space Science*, *8*(4), e2020EA001153. https://doi.org/10.1029/2020ea001153

Zhao, Z., Kravtsov, V., Wang, Z., Zhou, Z., Dou, L., Huang, D., et al. (2025). Applications of ultrafast nano-spectroscopy and nano-imaging with tip-based microscopy. *eLight*, *5*, 1. https://doi.org/10.1186/s43593-024-00079-1

Zhou, R. (2026). Data for "Nanophase iron of new nano-lamella and zoned morphology discovered in a lunar meteorite". *Mendeley Data*. https://doi.org/10.17632/rdn4889sxv.2

Zou, Y.-L., Liu, J.-Z., Liu, J.-J., & Xu, T. (2004). Reflectance spectral characteristics of lunar surface materials. *Chinese Journal of Astronomy and Astrophysics*, *4*(1), 97–104. https://doi.org/10.1088/1009-9271/4/1/97